Title
Interannual Atmospheric Variability Affects Continental Ice Sheet Simulations on Millennial Time Scales

Journal
Journal of Climate, 21(22)

ISSN
0894-8755 1520-0442

Authors
Pritchard, Michael S
Bush, Andrew B. G
Marshall, Shawn J

Publication Date
2008-11-01

DOI
10.1175/2008JCLI2327.1

Interannual Atmospheric Variability Affects Continental Ice Sheet Simulations on Millennial Time Scales

MICHAEL S. PRITCHARD

Scripps Institution of Oceanography, University of California, San Diego, La Jolla, California

ANDREW B. G. BUSH

Department of Earth and Atmospheric Sciences, University of Alberta, Edmonton, Alberta, Canada

SHAWN J. MARSHALL

Department of Geography, University of Calgary, Calgary, Alberta, Canada

(Manuscript received 15 November 2007, in final form 8 April 2008)

ABSTRACT

To inform the ongoing development of earth system models that aim to incorporate interactive ice, the potential impact of interannual variability associated with synoptic variability and El Niño–Southern Oscillation (ENSO) at the Last Glacial Maximum (LGM) on the evolution of a large continental ice sheet is explored through a series of targeted numerical modeling experiments. Global and North American signatures of ENSO at the LGM are described based on a multidecadal paleoclimate simulation using an atmosphere–ocean general circulation model (AOGCM). Experiments in which a thermomechanical North American ice sheet model (ISM) was forced with persistent LGM ENSO composite anomaly maps derived from the AOGCM showed only modest ice sheet thickness sensitivity to ENSO teleconnections. In contrast, very high model sensitivity was found when North American climate variations were incorporated directly in the ISM as a looping interannual time series. Under this configuration, localized transient cold anomalies in the atmospheric record instigated substantial new ice formation through a dynamically mediated feedback at the ice sheet margin, altering the equilibrium geometry and resulting in a bulk 10% growth of the Laurentide ice sheet volume over 5 kyr.

1. Introduction

Although high-frequency climate variability on the annual to subannual scale is reasonably well understood, there is an ongoing effort to account for observed low-frequency climate variability on interdecadal to millennial scales. A recent approach that has helped to address this problem is the incorporation of higher-frequency external forcing mechanisms into models of lower-frequency processes. Several such studies have provided useful insight into the evolution of slow modes in the ocean (e.g., Goosse and Renssen 2004), in the coupled atmosphere–ocean system (e.g., An and Wang 2005; van der Avoird et al. 2002; Schneider and Comuelle 2005; Newman et al. 2003), and in solid earth systems (e.g., Berger and von Rad 2005). It has become apparent from such studies that the influence of higher frequency processes on low-frequency climate variability is often not well represented stochastically. Rather, the well-defined spatial and temporal patterns of higher frequency phenomena (such as baroclinic eddies in the atmosphere) result in a coherent regional forcing of low-frequency climate variability that is fundamentally nonrandom even though they act on disparate time scales.

In contrast, there is a relative absence of high to low frequency coupled studies that deal with cryospheric processes. However, this technique has considerable potential for untangling the dynamic history of massive continental ice sheets in the earth's past since glacial inception (accumulation) and glacial demise (ablation)

Corresponding author address: Michael S. Pritchard, Scripps Graduate Department, Mail Code 0224, 9500 Gilman Drive, La Jolla, CA 92093-0224.
E-mail: mikepritchard@ucsd.edu

DOI: 10.1175/2008JCLI2327.1

are ultimately determined by high frequency atmosphere–ocean processes. Initial progress has been made by forcing thermomechanical ice sheet models (ISMs) with seasonally varying climatological fields derived from general circulation models (GCMs). This method has proven to be instrumental in producing reconstructions of the Laurentide ice sheet at the Last Glacial Maximum (LGM) (e.g., Marshall et al. 2002; Huybrechts et al. 2004) and has been used to investigate the fate of the Greenland ice sheet (Otto-Bliesner et al. 2006). However, this approach to ice sheet modeling may be limited by the fact that it only takes into account a single frequency of external atmospheric variability: the annual cycle.

However, as is the case in modern climate, interannual frequencies are likely to have played at least some role in glacial climates. Of particular note, El Niño–Southern Oscillation (ENSO) appears to have been present in the LGM climate (Tudhope et al. 2001) and because in contemporary climate it has a detectable impact on Arctic cryospheric processes (Slonosky et al. 1997; Mysak et al. 1996), it is likely to have affected glaciated regions in the past. ENSO signatures have been observed in tropical sea surface temperature proxies (Tudhope et al. 2001; Stott et al. 2002), as well as in recent paleoclimate atmosphere–ocean general circulation model (AOGCM) simulations (Rosenthal and Broccoli 2004; Bush 2007; Peltier and Solheim 2004). It has been shown that tropical SSTs at the LGM play a major role in the development of atmospheric teleconnection patterns over North America, with significant regional mass balance implications for the Laurentide ice sheet (Yin and Battisti 2001; Rodgers et al. 2004). In this study, analysis of temperature and precipitation anomalies associated with ENSO at the LGM based on a multidecadal AOGCM simulation confirm that the net effect of El Niño and La Niña anomalies over North America were sufficiently strong to impact millennial-scale ice sheet mass balance.

ENSO variability is only one component of the interannual spectrum. However, the physical interaction between an ice sheet and interannual atmospheric variability is very multiscale in space and time. Targeted numerical modeling experiments offer the opportunity to experiment with different subsets of this full multiscale interaction to identify potential thresholds of sophistication in the atmospheric forcing that explain different aspects of the overall ice sheet response. In this study, we gradually phase in components of interannual atmospheric forcing to investigate the relative sensitivity of a thermomechanic ice sheet model to 1) the persistent (phase and annually averaged) component of ENSO, 2) seasonally modulated but phase-averaged ENSO forcing, and 3) fully interannual forcing that includes transient synoptic variability and phase transitions between ENSO extrema.

Section 2 provides some background on ENSO teleconnections and a description of the numerical models and the simulation design. Section 3 describes the teleconnection patterns associated with simulated LGM ENSO events and the impact of stationary features on the Laurentide ice sheet. Results from the hierarchy of ice sheet simulations are presented in section 4.

2. Background

Atmospheric teleconnections over North America associated with ENSO arise from a number of interconnected dynamic processes that are likely to have been different in the earth's past. A variety of modern observations indicate that, during boreal wintertime, Alaska and western Canada experience warmer weather during El Niño while cooler, wetter conditions prevail over the eastern seaboard (Rasmusson and Carpenter 1982). Modest regional extratropical teleconnections also exist during summer but are generally weaker. Changes in moisture and temperature are accompanied by large-scale spatial anomalies in the midtropospheric geopotential height field that appear to be associated with the propagation of atmospheric planetary waves excited during El Niño, which may give rise to the Pacific–North American (PNA) pattern (Straus and Shukla 2002). Recent studies on the dynamics of ENSO teleconnections have investigated the effects of transient eddies, diabatic cooling processes (DeWeaver and Nigam 2004; Trenberth et al. 2002), and sources of nonlinear ENSO variability (e.g., Hannachi 2001; Wu and Hsieh 2004), all of which likely contribute to the development of preferred modes of atmospheric variability over North America.

a. Atmosphere–ocean GCM

The atmosphere–ocean model that we use is a combination of the hybrid spectral atmospheric GCM of Gordon and Stern (1982) and a three-dimensional finite difference primitive-equation ocean GCM (Bryan 1969; Pacanowski et al. 1991), both of which were developed at the Geophysical Fluid Dynamics Laboratory (GFDL). The atmospheric model has 14 vertical levels using the terrain-following σ-coordinate system with horizontal resolution limited by rhomboidal truncation at zonal wavenumber 30, whereas the oceanic component has 15 variably spaced vertical levels with a horizontal resolution of 2° latitude and 3.62° longitude. Oceanic vertical mixing is parameterized using the Richardson number scheme of Pacanowski and Philander (1981) and sea ice is modeled after Fanning and

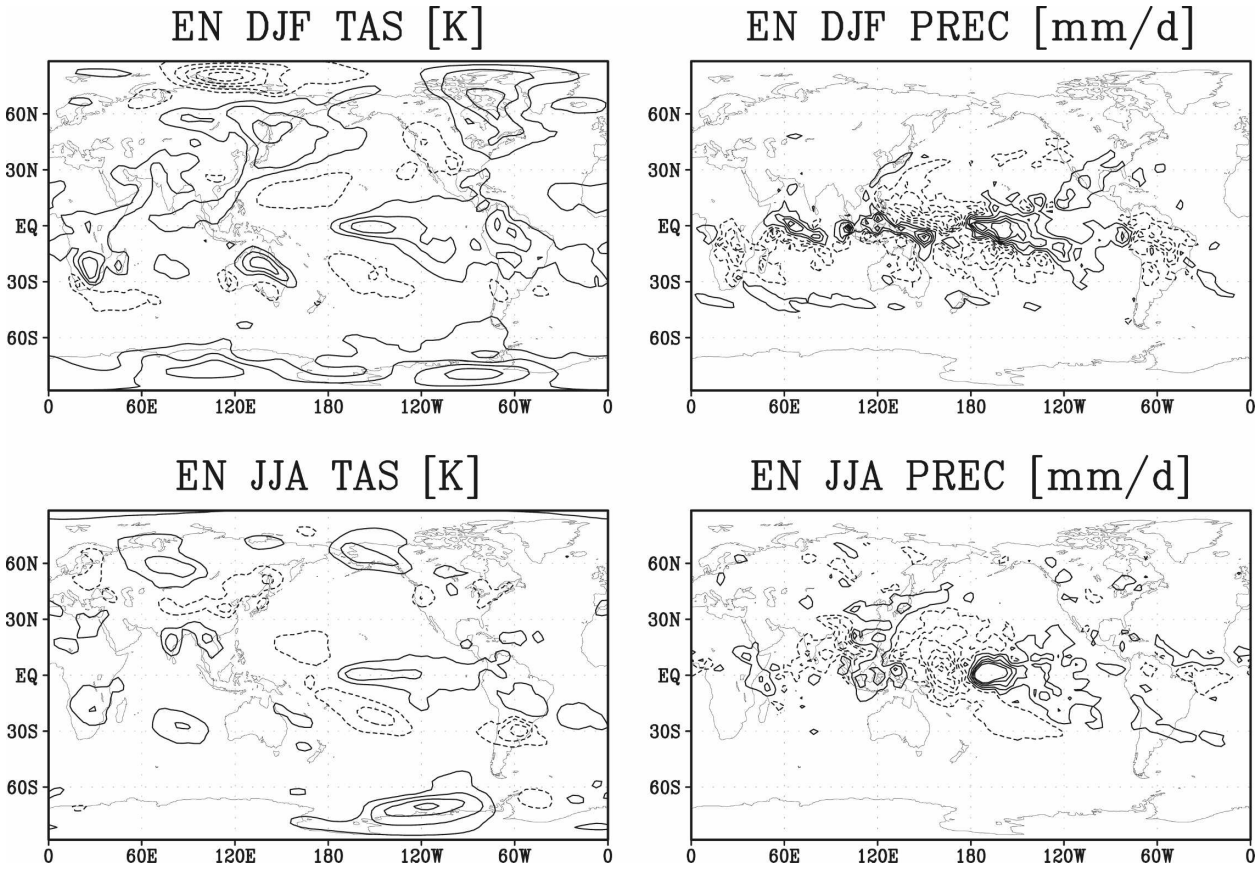

FIG. 1. Global DJF El Niño anomalies as simulated by the GFDL AOGCM for present-day conditions. El Niño composite anomalies are shown for (left) the near-surface air temperature (contour intervals are 0.3 K) and (right) precipitation (contour intervals are 0.6 mm day^{-1}). The zero contour line has been omitted to highlight anomalies; negative contours are dashed.

Weaver (1996). Carbon dioxide is set to 200 ppm, and reconstructed ice sheet topography is from Peltier (1994). The land surface albedo is from CLIMAP (1981), and sea level is set to 120 m below present-day values (Fairbanks 1989). Orbital parameters are from Berger and Loutre (1991). There is no dust in the model. The spinup time for the wind-driven circulation was 15 years, which is an appropriate duration for this vertical mixing configuration (Bush and Philander 1999). Simulations were run on an SGI Origin 2400 (six processors), and the run time is about one simulated year per 24 hours integration.

The GFDL AOGCM produces realistic ENSO variability in response to present-day climatological forcing (Bush 2007). The definition of El Niño (La Niña) in this study is the requirement that 5-month running mean SSTs within a box in the equatorial Pacific (Niño-3.4 region: 5°N–5°S, 120°–170°W) exceed a threshold departure of 0.4°C above (below) climatological conditions (Trenberth 1997). Figure 1 shows December–February (DJF) El Niño anomalies of near-surface air temperature (TAS) and precipitation (PR) extracted from a 60-yr control simulation of modern climate. The regional distribution of El Niño temperature and precipitation anomalies in the AOGCM is largely in agreement with observations from the National Centers for Environmental Prediction–National Center for Atmospheric Research (NCEP–NCAR) reanalysis (Fig. 2; Kalnay et al. 1996) although the magnitude of the thermal response is underestimated, most likely because of diffusive effects associated with the relatively coarse atmospheric model resolution. In addition to the classical eastward motion of the tropical Pacific warm pool, areas observed today that experience drought during El Niño, such as South Africa, Australia, Indonesia, and the Amazon Basin, are congruous with warm and dry El Niño anomalies in the AOGCM simulation. In comparison to previous simulations, the Richardson number vertical mixing scheme in the ocean GCM has enabled the GFDL coupled model to simulate realistic modern ENSO variability (Pacanowski and Philander 1981). Although some underestimation of regional

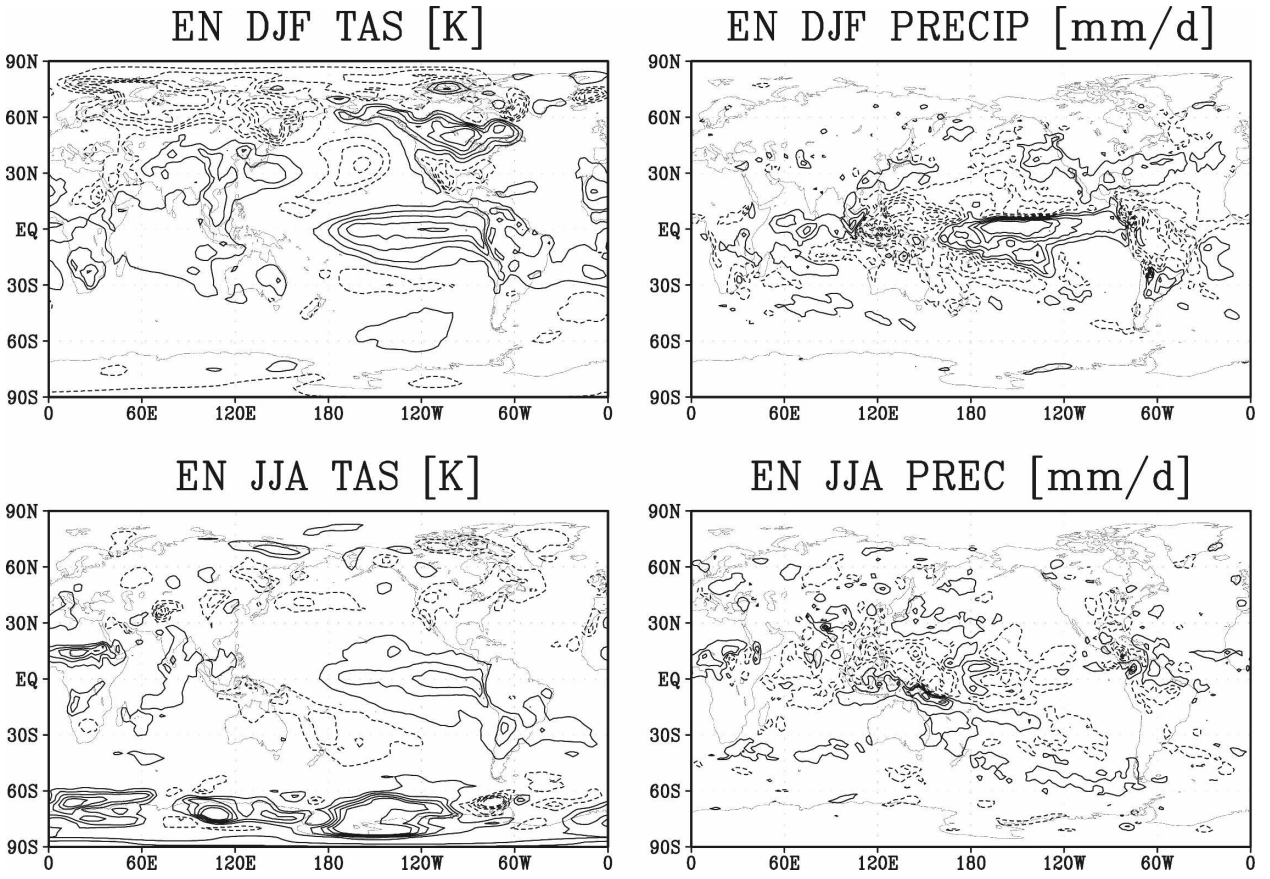

FIG. 2. As in Fig. 1 but for observed El Niño anomalies computed from years 1948 to 2006 of the NCEP–NCAR reanalysis.

warming occurs over the eastern tropical Pacific and there is a bias in the position of the wintertime warm anomaly over North America, the overall quality of the simulated present-day ENSO teleconnection patterns is quite reasonable compared to other coupled AOGCMs (AchutaRao and Sperber 2002).

The climate of the Last Glacial Maximum has been studied extensively using a variety of coupled AOGCMs (e.g., Bush and Philander 1998, 1999; Peltier and Solheim 2004; Shin et al. 2003), among which there has been a preliminary consensus concerning the La Niña–like mean state of the LGM climate, although uncertainties remain regarding subtropical and tropical ocean conditions (Hostetler et al. 2006). Here a 60-yr section of an LGM simulation described in Bush (2007) is analyzed. In this simulation there is a global average surface cooling of 4.3°C compared to present-day conditions, primarily due to cooling over the North American and Eurasian ice sheets, both of which were incorporated in the AOGCM using Peltier's (1994) ICE-4G reconstruction. As in some previous simulations, changes in climatological winds at the LGM include a strengthening of the tropical Pacific easterlies (Shin et al. 2003; Peltier and Solheim 2004), increased cyclonic activity over the northwest Atlantic (Bush and Philander 1999; Hall and Chan 2004), and a weakening of the South Asian summer monsoon (Bush 2002; Zhao et al. 2003). As found in all GCM studies, the Laurentide ice sheet has a significant effect on the low-level circulation over North America (Fig. 3). The massive topography of the Laurentide ice sheet acts as an obstacle to low-level atmospheric flow, effectively splitting the westerly midlatitude jet stream into two branches that circumnavigate the ice sheet perimeter to the north and to the south. The fast-flowing northern and southern branches of this midlatitude "split jet stream" recombine downstream of the ice sheet into a single broad band of intense southwesterly wind over the eastern North Atlantic. A strong anticyclone is superimposed on these winds over the cold ice sheet interior, as is observed today over the Greenland and Antarctic ice sheets owing to the presence of climatological cold core highs.

A hierarchy of ice sheet simulations is presented in this study, with each simulation driven by varying components of interannual atmospheric forcing that were extracted from the AOGCM LGM simulation. To in-

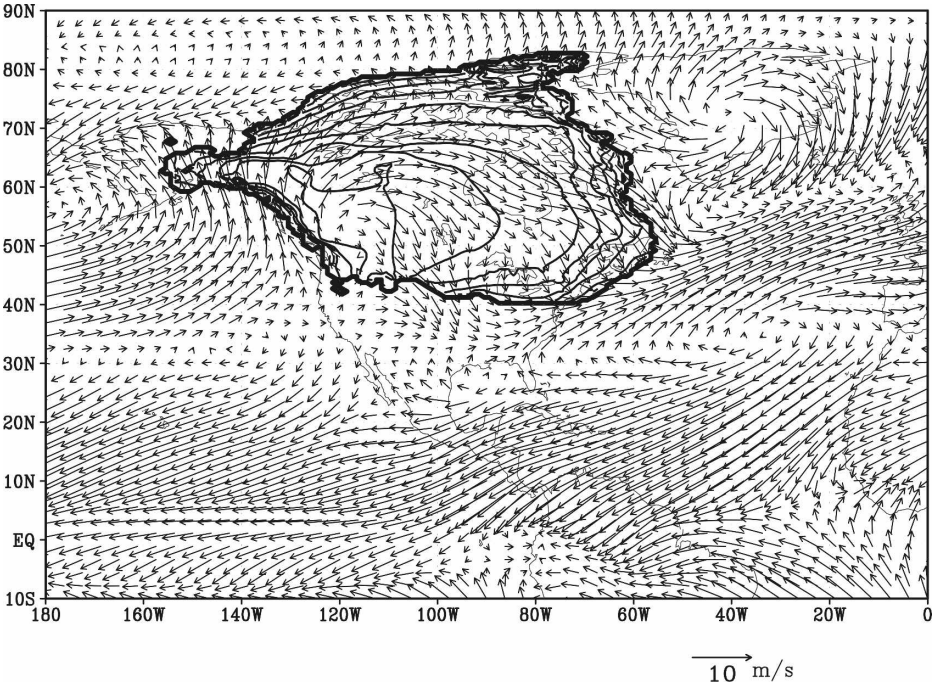

FIG. 3. Climatological near-surface winds in the vicinity of the Laurentide ice sheet. The contours show Laurentide ice sheet topography (contour interval 250 m).

vestigate the effects of ENSO phase extrema (and their mean) on Laurentide ice sheet dynamics at the LGM, composite temperature and precipitation fields were isolated for those months in the AOGCM matching the El Niño–La Niña tropical SST criteria of the Niño-3.4 region (Trenberth 1997). Details of the composite anomaly maps are discussed in section 3. It is prudent to note that the definition of El Niño and La Niña months in the tropical Pacific (i.e., SST anomalies exceeding 0.4°C for 6 months) gives rise to a nonlinear relationship between associated El Niño and La Niña anomalies in the extratropics such that the average of the composite anomalies is nonzero, as observed in extratropical ENSO teleconnections today. This fact leads to the possibility of a persistent interannual forcing on ice dynamics due to phase-averaged ENSO in these ice sheet simulations. In contrast to the above simulations, the ice sheet simulations forced by fully interannual atmospheric forcing make use of the entire 60-yr monthly time series of precipitation and temperature in the AOGCM record.

b. Ice sheet model

The numerical ISM used in this study is a three-dimensional thermomechanical formulation similar to that developed by Huybrechts (1990). We employ this model to represent the Laurentide ice sheet on a North American domain with 20 vertical levels, a longitudinal resolution of 1° and a latitudinal resolution of 0.5°. Detailed discussions of the model equations and parameterizations are presented in Marshall and Clarke (1997) and Marshall et al. (2002). Briefly, the model employs a set of rheologically constrained conservation equations for energy, mass, and momentum in order to simulate the large-scale diffusion of mass (Mahaffy 1976) and heat (Jenssen 1977) within the ice sheet. The ice flows according to viscous creep dynamics (neglecting the effects of longitudinal stresses), with a parameterization for basal sliding, introduced as a basal boundary condition and activated when the ice is warm based and lubricated by basal meltwater (Marshall et al. 2002). Evolving ice loads are interactively coupled to an isostatic mantle lithosphere model based on Wu and Peltier (1982) and Peltier (1985). Near-surface temperature fields from the atmospheric model are used to drive snow and ice melt through a monthly positive-degree-day (PDD) melt parameterization (e.g., Huybrechts et al. 2004). PDDs are computed consistently in all ice sheet simulations, assuming normal monthly temperature distributions with a standard deviation of 5 K. Several other parameterizations are employed to represent various uncertain processes in ice sheet modeling, such as marine iceberg calving, and are discussed in Marshall et al. (2000). These parameterizations nec-

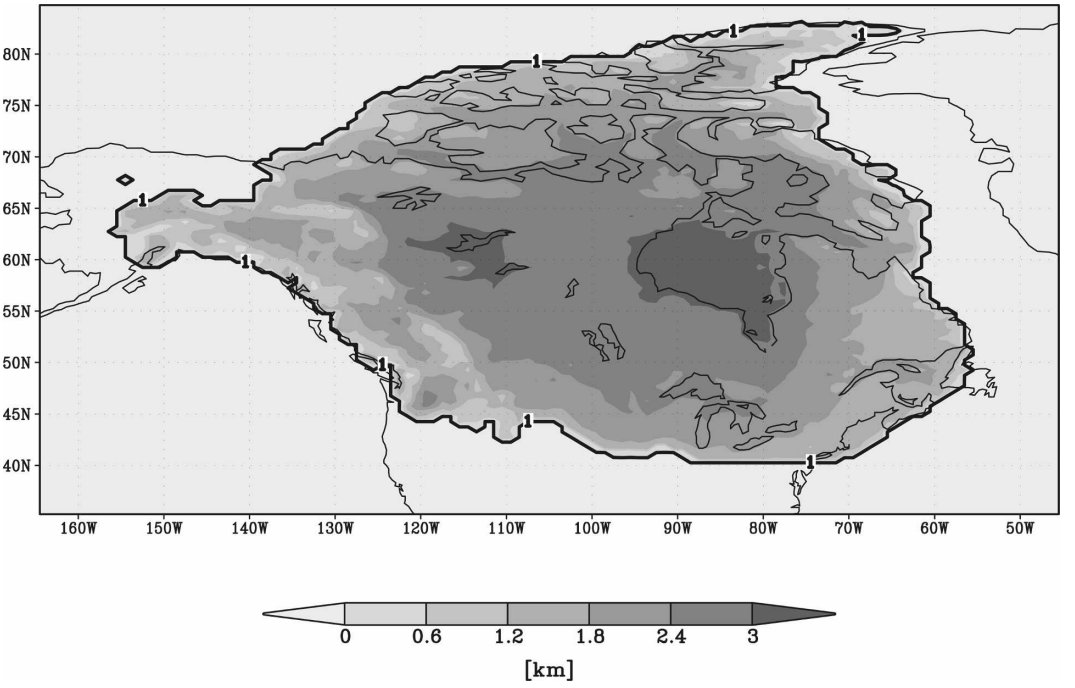

FIG. 4. Initial ice thickness state of the Laurentide ice sheet, used to initialize the Marshall and Clark (2002) ISM for all ice sheet simulations.

essarily have a significant effect on overall ice evolution (Marshall et al. 2002); we impose a parameter suite that has proven capable of growing ice over North America within the constraints of the reconstructed Laurentide ice sheet geometry.

The large-scale dynamics of the ice sheet are strongly controlled by climatological boundary conditions imposed at the ice sheet surface. Owing to the seasonality of ablation and accumulation, this forcing is conventionally imposed through a set of monthly mean temperature and precipitation fields representing a climatological annual cycle. These are horizontally downscaled from the coarse atmospheric model grid to the higher-resolution ice sheet model grid using 2D cubic spline interpolation. The temperature field is specified for a given pressure level in the atmosphere and linearly interpolated to the evolving ice sheet surface by assuming a constant atmospheric lapse rate of $-6°C$ km^{-1}.

c. Ice sheet simulations

All ice sheet model experiments were initialized with a LGM Laurentide ice sheet thickness distribution obtained from the ISM simulation of Marshall and Clark (2002) with a linear vertical temperature profile. Internal temperatures and ice geometry were subsequently equilibrated to the AOGCM LGM annual climatology over the course of a 57-kyr spinup simulation forced by seasonal temperature and precipitation climatology from the AOGCM. Since the initial ice configuration differed somewhat from the ICE-4G reconstruction used in the AOGCM run, some mass readjustment occurred during this spinup process. The end state of the spinup simulation was used to initialize each of the subsequent four simulations that follow, and is shown in Fig. 3 (ice topography) and Fig. 4 (ice thickness). Ice thickness peaks at 3500 m over the Hudson Bay region, with outward channelized flow from a high altitude cordilleran dome that reaches peak speeds of 400 m yr^{-1} in regions of topographically steered ice convergence.

To investigate the effects of different modes of interannual atmospheric variability on ice sheet dynamics, we conducted a hierarchy of ice sheet simulations forced by incrementally complete components of the interannual AOGCM signal. The results of these experiments were interpreted relative to a control run (CONT) in which the Laurentide ice sheet dynamics were forced by the monthly LGM climatology from the 60-yr AOGCM record; the ice sheet is stable to this forcing.

In the first experiment (ENLN), the ice sheet sensitivity to the persistent (phase and annually averaged) component of interannual ENSO variability was investigated. In this simulation the imposed LGM annual cycle climatology was perturbed by an average of the El Niño (EN) and La Niña (LN) annual climate anoma-

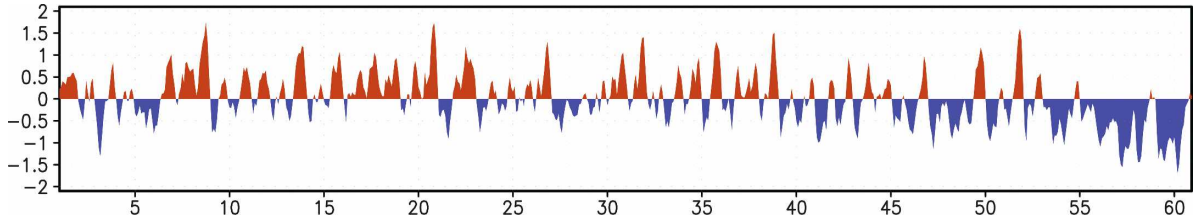

FIG. 5. ENSO index in the LGM AOGCM simulation (time series of the SST anomaly in the Niño-3.4 region of the tropical Pacific).

lies. The ENLN climate anomaly perturbation is not meant to represent reality; rather, by design it effectively amplifies the regions where the North American teleconnections from the two ENSO phase extrema mutually interfere to produce a net climate forcing with a distinct spatial pattern that has consequences for ice evolution. This choice of climate forcing is made as a means of bracketing a potential upper limit for ice sheet sensitivity to this component of interannual ENSO variability within the tested confines of an ice sheet model forced by purely annual-cycle climate forcing.

The next experiment (ENLN-S) goes a step further, by incorporating seasonal modulation of ENSO into the climate forcing, in order to determine whether this enhances or diminishes the ice sheet sensitivity relative to ENLN through interaction of ENSO seasonality with the seasonal cycle of cryospheric mass balance. This is achieved by perturbing each month of the annual cycle climate forcing independently by the mean of monthly climatological El Niño and La Niña composite anomalies.

ENLN and ENLN-S are in contrast to a third experiment (INTERANN), which breaks tradition with conventional ice sheet modeling practices by using a fully interannually varying climate record. This allows an exploration of ISM sensitivity to the full LGM ENSO oscillation, including transitions between extrema and year-to-year synoptic regional anomalies in the AOGCM. In INTERANN the ice sheet is forced by looping a monthly climate record spanning the entire 60-yr AOGCM simulation. Interestingly, the ice response to the phase-averaged components of ENSO turns out to be masked in this simulation by a regional dynamical interaction between ice marginal advance and transient ice formation over high topography during anomalously cold events in the interannual climate record. This result motivated a fourth and final experiment (INTERAND) to determine whether this mechanism is sensitive to the spatial coherence of synoptic climate anomalies in the interannual atmospheric forcing fields. In INTERAND, the interannual variations in near-surface atmospheric temperature (T) and precipitation (P) in the AOGCM record were replaced with spatially and temporally decorrelated random noise (T', P'),

$$T'(x, y, m, t) = U[\overline{T}(x, y, m) - \sigma_T(x, y, m), \overline{T}(x, y, m) + \sigma_T(x, y, m)] \quad (1)$$

$$P'(x, y, m, t) = U[\overline{P}(x, y, m) - \sigma_P(x, y, m), \overline{P}(x, y, m) + \sigma_P(x, y, m)], \quad (2)$$

where (x, y) indexes the horizontal grid point, m is the month, t is the year, overbars denote averaging in t, $\sigma_{T,P}$ are the standard deviations (in t) of temperature and precipitation: $U(\phi_1, \phi_2)$ is a uniform random number generator for the range of numbers (ϕ_1, ϕ_2); U was computed independently for each (x, y, m, t).

3. ENSO at the LGM

A time series of the SST anomaly in the Niño-3.4 region of the tropical Pacific for the AOGCM is shown in Fig. 5. Of the total 744 simulated months, 152 (20%) met the El Niño criteria, and 159 (21%) met the La Niña criteria. The Niño-3.4 time series in the model shows realistic variability as well as an overall trend; computational expense of the AOGCM simulation (one model year per day) prohibits attribution of the latter to either centennial-scale variability or model drift.

Figure 6 shows the global temperature and precipitation teleconnections associated with El Niño. The extratropical thermal response to winter El Niño conditions simulated for the LGM was much more pronounced at high latitudes than for current conditions (cf. Fig. 1a), increasing in amplitude by a factor of 3 over the Antarctic and Arctic regions with a mean peak warming of 3°C over the Laptev and East Siberian Seas. Such extreme high-latitude teleconnections are consistent with prior studies of the LGM (Rodgers et al. 2003). Warming in the central tropical Pacific at the LGM is less than for modern El Niño conditions because of the extended cold tongue of the LGM mean climate. Like today, warm and dry conditions prevail

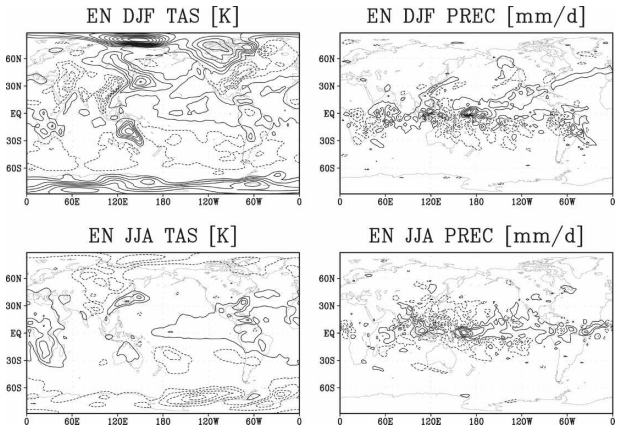

FIG. 6. As in Fig. 1 but for LGM El Niño conditions.

during El Niño over Australia and South Africa. However, cooling and a large increase in precipitation occur over eastern Brazil at the LGM, a result that is opposite to what is observed during modern El Niño. This result is consistent with proxy evidence from this region indicating anomalously cool and wet conditions during this time period (Wang et al. 2004).

The teleconnection patterns in Fig. 6 can be understood in terms of dynamic changes in the atmospheric circulation. In the vicinity of the Laurentide ice sheet annually averaged temperature, precipitation, and wind anomalies during El Niño (Fig. 7) indicate that a large-scale atmospheric warming of 1°C occurs over the northern margin of the Laurentide ice sheet, caused by an intensification of the northern branch of the split jet and a consequent increase in advection of warm, low-latitude air. An anticyclonic flow pattern is visible in the wind anomalies over the ice sheet and this increases the advection of cool air onto the southeastern Laurentide ice sheet margin resulting in a 1°C cooling over the region during El Niño. The intensification of the northern branch of the split jet stream also acts to increase orographic precipitation rates over the southern coast of Alaska (Fig. 7b). In contrast, weakening of the southern branch of the jet reduces orographic precipitation along the western coast and along much of the southern margin of the ice sheet. Precipitation rates are also enhanced during El Niño over the Baja Peninsula and within the Atlantic storm track region where El Niño temperature anomalies act to enhance the local atmospheric baroclinicity, particularly during boreal winter months (Bromwich et al. 2004). As is the case today, LGM La Niña composite anomalies (Fig. 8) are qualitatively opposite (but quantitatively weaker) compared to El Niño and are also consistent with dynamic atmospheric readjustments evident in the wind field.

The structures of the annually averaged El Niño and

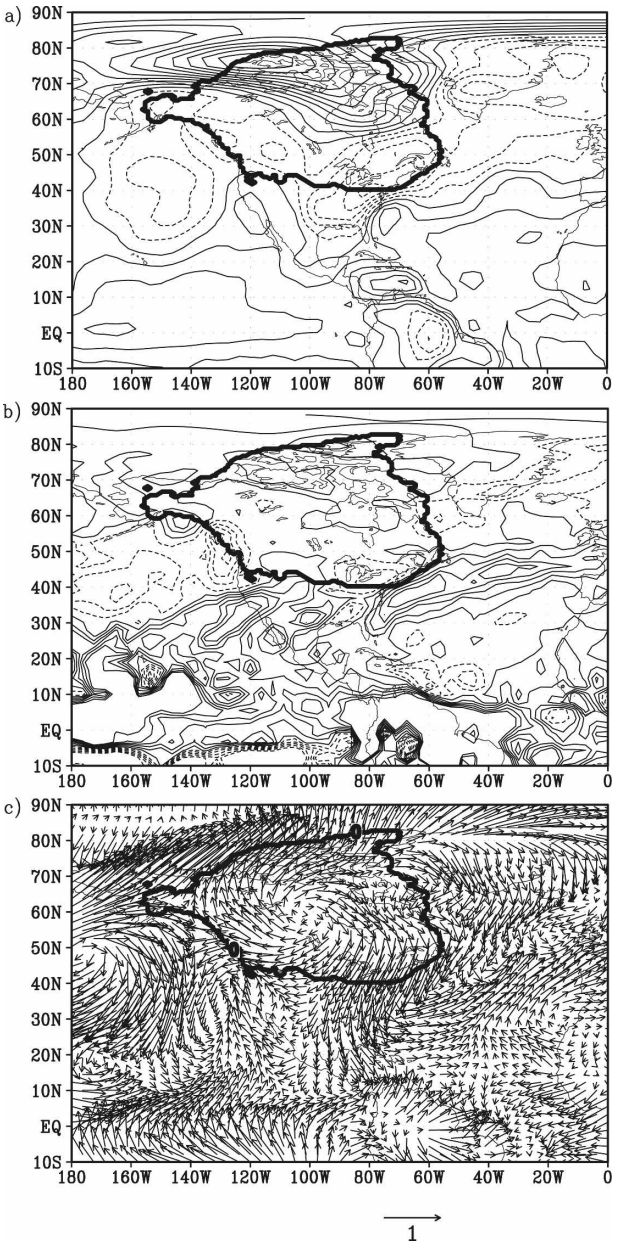

FIG. 7. Annually averaged El Niño anomalies from the AOGCM LGM climatology, shown over the Laurentide ice sheet, for (a) the near-surface air temperature, (b) precipitation, and (c) the near-surface wind field. The temperature contour interval is 0.2 K and the precipitation contour interval is 0.1 mm day^{-1} (precipitation anomalies higher than 0.5 mm day^{-1} are omitted to highlight only the variability in the vicinity of the ice sheet).

La Niña composite anomaly maps shown in Figs. 7 and 8 shed light on the pattern of mass balance response in the ENLN ice sheet simulation (section 4a). However, these annual average climate perturbations are dominated by the strong winter El Niño atmospheric responses, and thus mask the rather different summer-

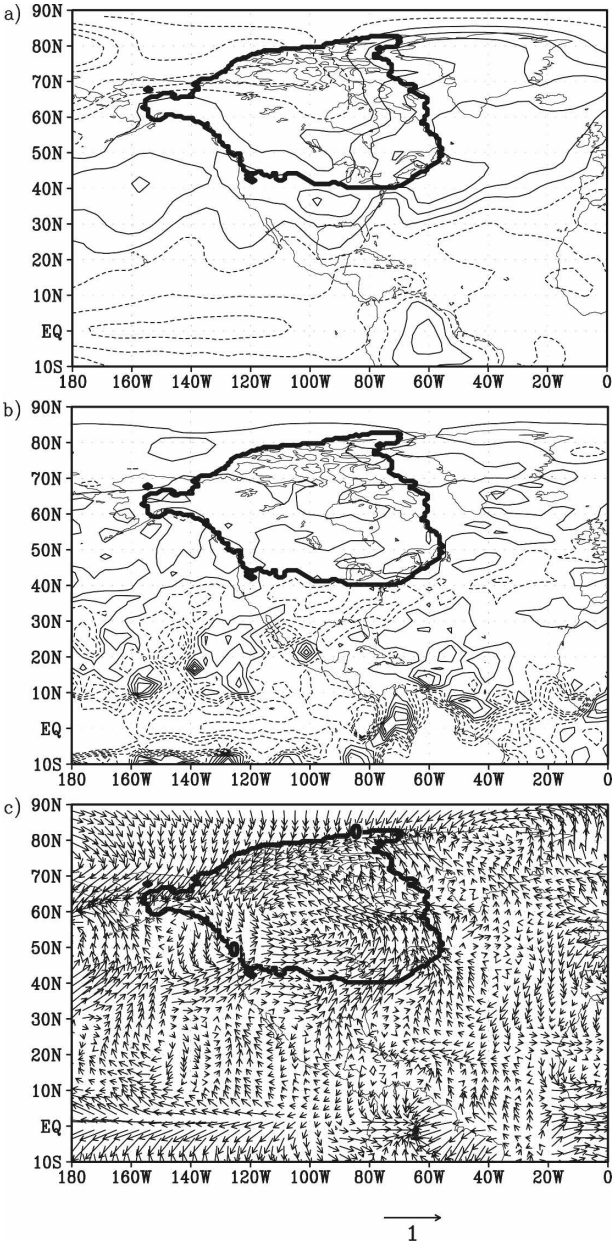

FIG. 8. As in Fig. 7 but for LGM La Niña conditions.

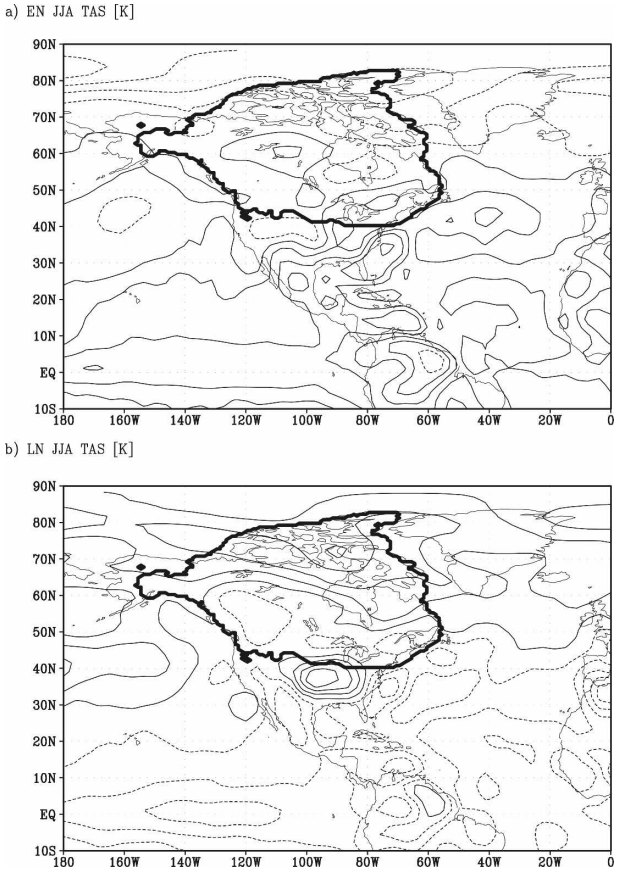

FIG. 9. LGM (a) El Niño and (b) La Niña composite anomaly maps showing the change in near-surface air temperature during summer months only (JJA): contour interval is 2 K.

time teleconnection features that underlie the ice sheet response in the ENLN-S simulation (in which the incorporation of seasonal variability in the phase-averaged climate perturbation constituted a more faithful representation of the ablation season). Much like today, the summertime North American thermal teleconnections associated with El Niño and La Niña at the LGM are weaker and of a different character for June–August (JJA) than for the annual average. For EN conditions in JJA (Fig. 9, upper panel), there is a modest cooling along the northern margin, which is concentrated at the northeast, and a warm anomaly along the southeast margin; these features are opposite to those apparent in the annual mean EN composite (Fig. 7). The LN JJA composite (Fig. 9, lower panel) shows warming over the northern margin and in a localized region along the central southern margin, as well as cooling at the southeast margin of the ice sheet.

4. Ice sheet simulation results

Results from the hierarchy of ice sheet model simulations are presented in order of increasing completeness in the spectrum of interannual variability incorporated into the climate forcing fields. The final state of each simulation is shown relative to the climatologically driven control case (CONT) in Fig. 10 and Fig. 12. Briefly, we find that the ice sheet is only weakly sensitive to persistent climate perturbations in the form of phase-averaged annual ENSO composite anomalies (ENLN). When the seasonal modulation of phase-averaged ENSO forcing is incorporated into the climate

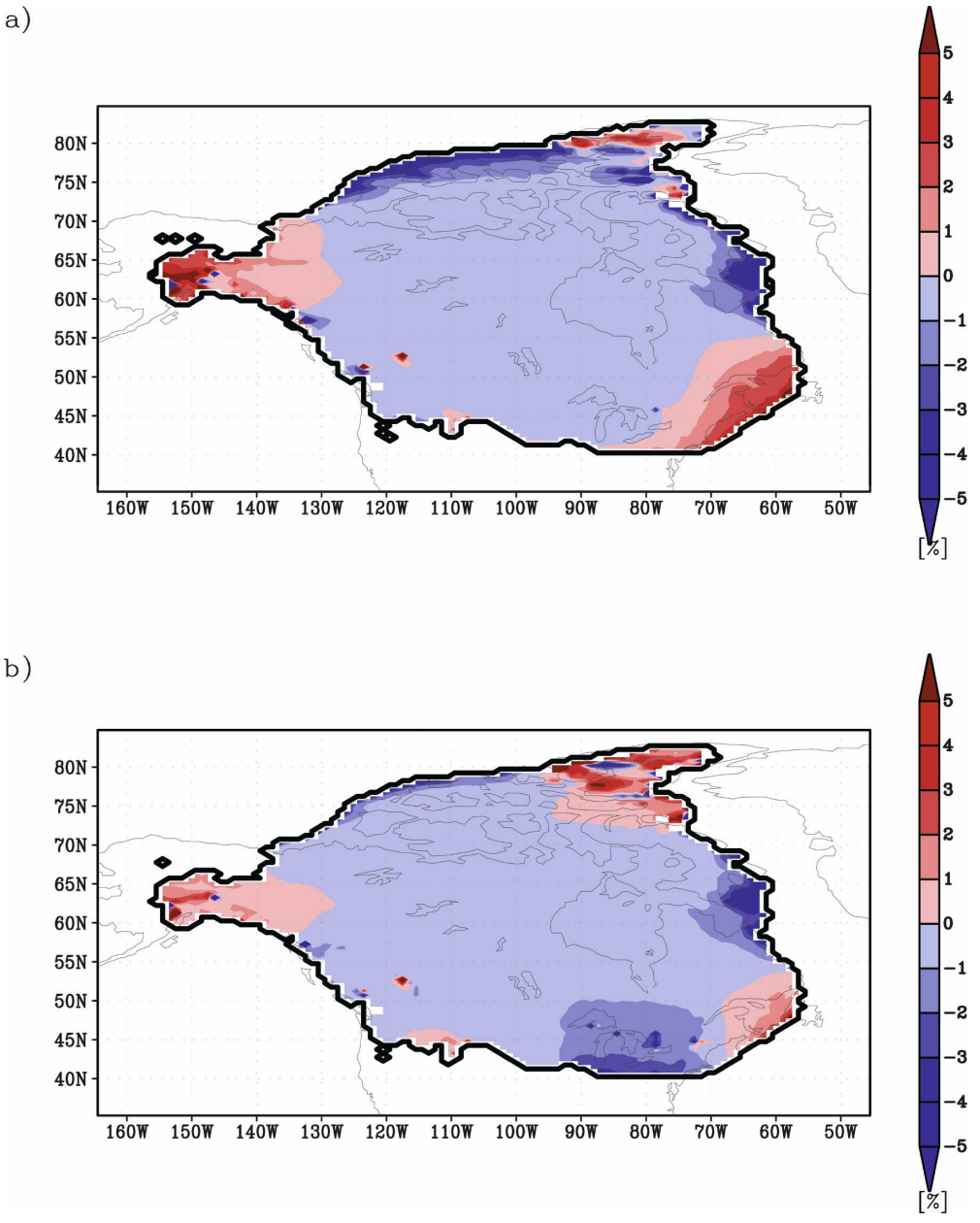

FIG. 10. Laurentide ice sheet thickness anomalies (percent change) for combined El Niño and La Niña LGM climatological forcing during two 5-kyr ice sheet simulations: (a) ENLN simulation in which ENSO seasonal variability was neglected and (b) ENLN-S simulation, which retains monthly variability in the LGM ENSO climate perturbation.

forcing (ENLN-S), the ice sheet sensitivity is damped further. However, upon full interannual forcing (INTERANN, INTERAND), a dramatic sensitivity and restructuring of the ice sheet is observed. A detailed discussion of each simulation follows.

a. Persistent phase-averaged ENSO forcing

Owing to the nonlinearity of the North American teleconnections associated with El Niño and La Niña, their combined effect on the mass balance of the Laurentide ice sheet at the LGM is nonzero [as is also the case for modern ENSO from observations; see Trenberth et al. (2002)]. Relative to the control simulation, the ice sheet simulation driven by persistent phase-averaged ENSO forcing (ENLN) results in a modest reduction of ice thickness along the northern ice sheet margin where a thinning of 50–100 m occurs, as well as off the southeastern coast of Baffin Island where ice

thins by as much as 200–300 m (Fig. 10a). The former effect is explained by the fact that the annually averaged warming of the northern jet branch during El Niño (Fig. 7) is higher in magnitude than the corresponding cooling in this region during La Niña (Fig. 8), resulting in net ablation over the northwestern ice margin for the phase average. The latter effect arises because the warm EN anomaly positively reinforces anomalously warm LN conditions in a region of reduced precipitation along the southeastern coast of Baffin Island; the consequent increase in ice ablation and decrease in accumulation results in strong net mass loss. A small ice gain of 30–60 m occurs along the southeast margin of the ice sheet, where the cold EN anomaly dominates LN warming and reduces the ablation rate. This modest sensitivity of the ISM response to phase-averaged ENSO perturbations is consistent with the findings of Rodgers et al. (2004).

b. Seasonally modulated phase-averaged ENSO forcing

Including seasonal variability in the ENSO climatological forcing fields (ENLN-S) yields an even smaller sensitivity in the ice sheet relative to ENLN. The dominant mass balance response is again ablative, but due to the incorporation of seasonal variability in ENLN-S, the ENSO forcing is weaker, and its spatial pattern is primarily controlled by the average of summertime thermal anomalies depicted in Fig. 9. As explained in section 3, these JJA ENSO teleconnections are markedly different than annual-average teleconnections. Summertime cooling during EN outweighs warming during LN at the northeast of the ice sheet, driving a net thickness gain. As in ENLN, the mean climate anomaly at the northwest margin results in net melting (LN warming here slightly surpasses EN cooling), although at a more modest rate. A new region of thinning is also evident in the ENLN-S simulation along the southern margin, owing to positively reinforcing regional warm anomalies here in both the EN and LN summertime teleconnections.

Based on this simulated response to perturbed annual cycle forcing, a quantitative estimate for the influence of the phase-averaged component of ENSO forcing on the ice sheet's mass balance may be made. Since the sensitivity of the ISM simulations to ENSO forcing is dominated by local ablation adjustments, which are prescribed in the model in proportion to the number of positive degree-days per month, we define the following sensitivity parameter:

$$S = \left(\frac{\mathrm{PDD}^{\mathrm{ann}}_{\mathrm{ENLN\text{-}S}}}{\mathrm{PDD}^{\mathrm{ann}}_{\mathrm{CONT}}} - 1 \right) \times 100\%, \qquad (3)$$

where superscripts denote (annual) time averaging and subscripts distinguish simulations. Equation (3) expresses the anomalous number of positive degree-days associated with the phase-averaged ENSO teleconnection climate forcing as a percentage of the seasonal positive-degree-day annual cycle in the control simulation. The sensitivity parameter S as a function of latitude and longitude over the ice sheet indicates that there is net warming due to phase-averaged ENSO variability over the northwestern ice sheet ablation zone (Fig. 11). However, the corresponding increase in PDD is less than ~5% above the annual cycle PDD in this region. At the southeastern margin, net cooling due to ENSO extrema results in a decrease in PDD of ~5% of the background annual cycle.

c. Full interannual forcing

The pattern of ice sheet evolution in the 5-kyr INTERANN simulation, in which ice evolution was forced by a looping 60-yr record of LGM climate, was distinctly unlike the prior simulations forced every year by the same mean of ENSO phase extrema, and in which no change occurred in the ice sheet bulk geometry, net mass balance, or margin locations. Remarkably, allowing the climate forcing fields to vary interannually caused the ice sheet to expand toward a distinctly altered equilibrium geometry. Figure 12 shows the thickness change of the INTERANN simulation relative to CONT, at the end of the simulation. The ice sheet response in INTERANN was a marked thickening accompanied by an advance of the ice sheet on the southwest and northwest margins. The dominant feature of the 5-kyr simulation was the initial and rapid growth of a narrow domelike structure near the southwestern margin of the ice sheet atop the high altitude bed topography at the eastern edge of the cordillera. Ice thickened substantially in this region, attaining the highest altitudes of the entire ice sheet. Ice outflow from this dome raised the level of the ice sheet globally and contributed to an outward expansion of the western ice margin. A narrow band of new ice growth in these regions reached over 1 km in height.

Correlation analysis implicates precipitation and ice dynamics as mechanisms underlying the dramatic ice sheet response to interannual forcing. Figure 13 depicts the correlation between yearly tendencies in mass balance and yearly tendencies in accumulation and air temperature, computed as a function of space for a representative cycle of the 60-yr interannual climate forcing time series. Significant correlations ($R > 0.6$) are shaded. As expected, over the elevated ice sheet interior (accumulation zone) year-to-year variations in

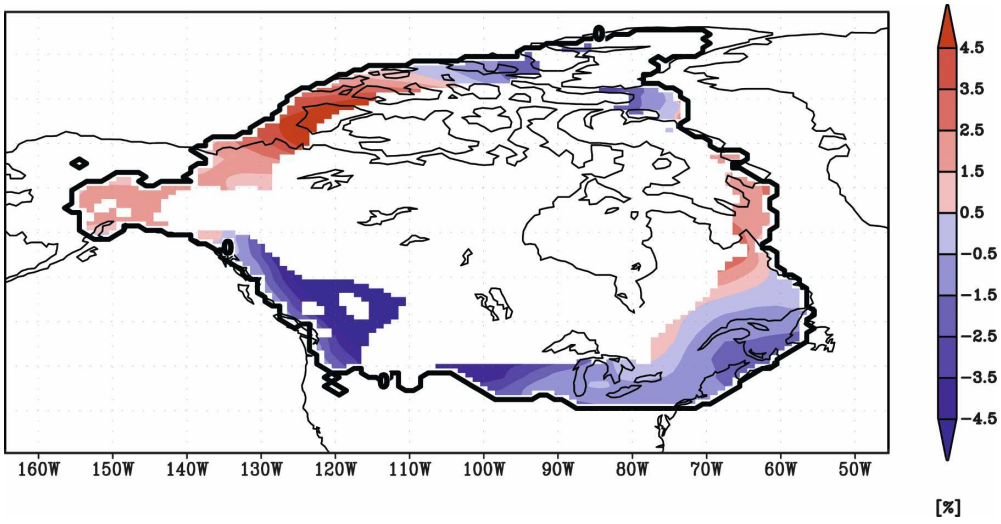

FIG. 11. Change in the number of annual positive degree-days due to phase-averaged interannual ENSO climate forcing in the ENLN-S ice sheet simulation, expressed as a percentage of the annual ablation cycle in the control simulation [Eq. (3)]. Shown only in the ice sheet ablation zone, that is, where $PDD^{ANN}_{CONT} > 5$.

annual mass balance are highly correlated with fluctuations in the distribution of precipitation (Fig. 13, left panel; $R > 0.9$). In contrast, an expected anticorrelation between yearly tendencies in local mass balance and JJA temperature is missing in the crucial western low-lying regions of the ice sheet. Although this anticorrelation between air temperatures and mass balance is robust along the southeastern, northern, and eastern ablation zones, there is no such relationship over the regions of dominant thickening during INTERANN (along the western margins). This rules out ablative mechanisms and suggests a dominant role of precipitation and ice dynamics in driving the rapid ice sheet expansion in this region.

Analysis of the basal velocity fields confirms that in the most sensitive regions of the ice sheet during INTERANN the dominant control on ice growth is a dynamical response to interannual climate forcing. This mechanism is illustrated in Fig. 14, which shows the expansion of the south cordilleran ice margin during the first year of the interannual record. Ice inception at previously ice-free cells adjacent to the margin occurs

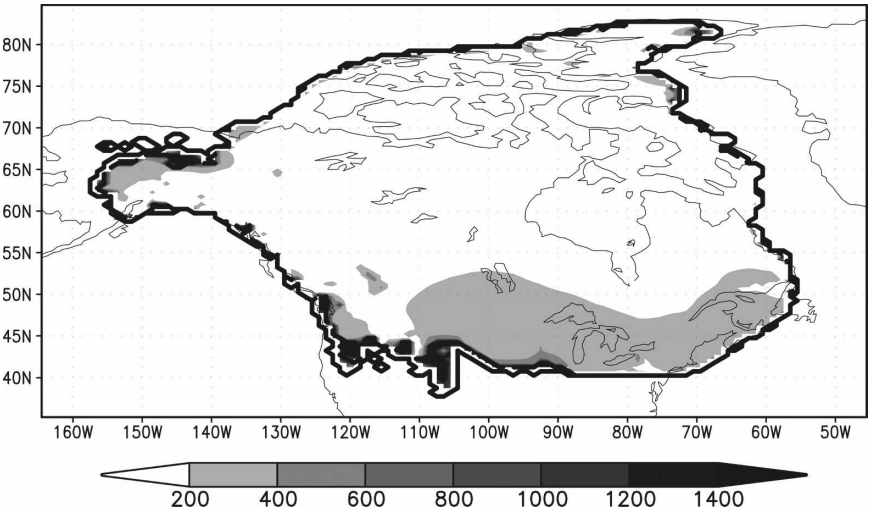

FIG. 12. Ice thickness anomaly relative to CONT for the INTERANN simulation, showing ice growth throughout the domain and concentrated along the western margins. A dominant feature is the growth of a new fingerlike outgrowth of ice atop the cordilleran range.

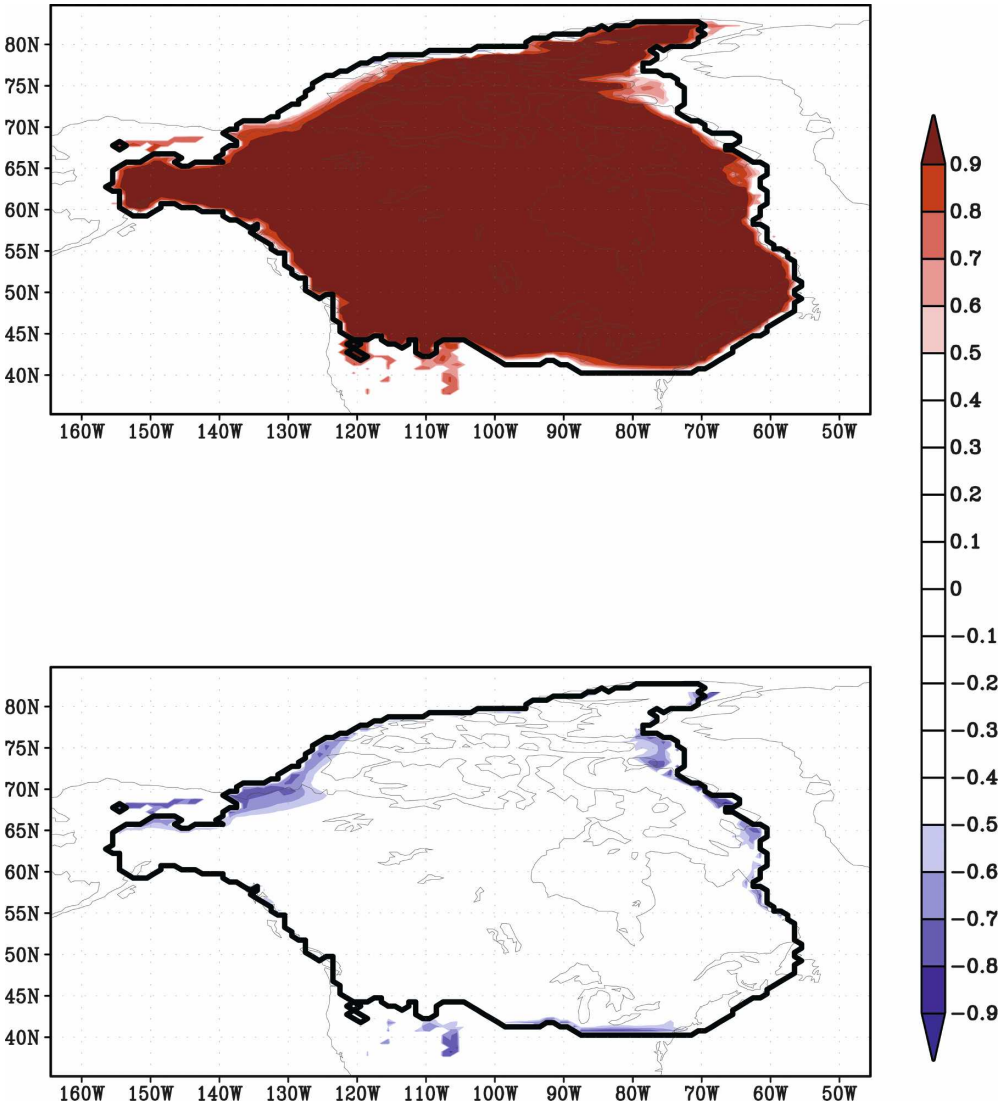

FIG. 13. Correlation coefficient R showing the strength of the linear relationship (top) between net mass balance tendencies and accumulation tendencies and (bottom) between net mass balance tendencies and air temperature tendencies, computed for a representative 60-yr cycle of the interannual climate forcing during the INTERANN simulation.

due to uncharacteristically cold summertime temperatures during this year (Fig. 14, upper panel). During the subsequent model year, the previously stable ice margin begins to advance, primarily through basal flow. Once triggered, this dynamic flux input facilitates ice growth in newly covered cells by contributing local ice thickness increases much higher than those caused by meteoric accumulation alone. Basal velocities are on the order of 50 m yr^{-1} at the southern extremity of the existing cordilleran margin (Fig. 14, bottom panel). This dynamic input has the capacity to stabilize new ice formed during cold extremes in the interannual record against counteracting ablation events later in the interannual record, the existence of which is evidenced by a lack of persistent ice growth in these cells when the ice sheet is forced with a climatological mean annual cycle. Where ice inception during anomalously cold events is sufficiently high to trigger this dynamic effect (i.e., at high altitudes), an expansion of the ice sheet margin occurs in the interannual simulation relative to the control. This mechanism also underlies the bulk shift toward a more massive equilibrium ice sheet volume in INTERANN relative to CONT: not only is the catchment area increased but, as ice elevates to cooler atmospheric environments in newly occupied cells from dynamic input, local ablation is suppressed and the overall

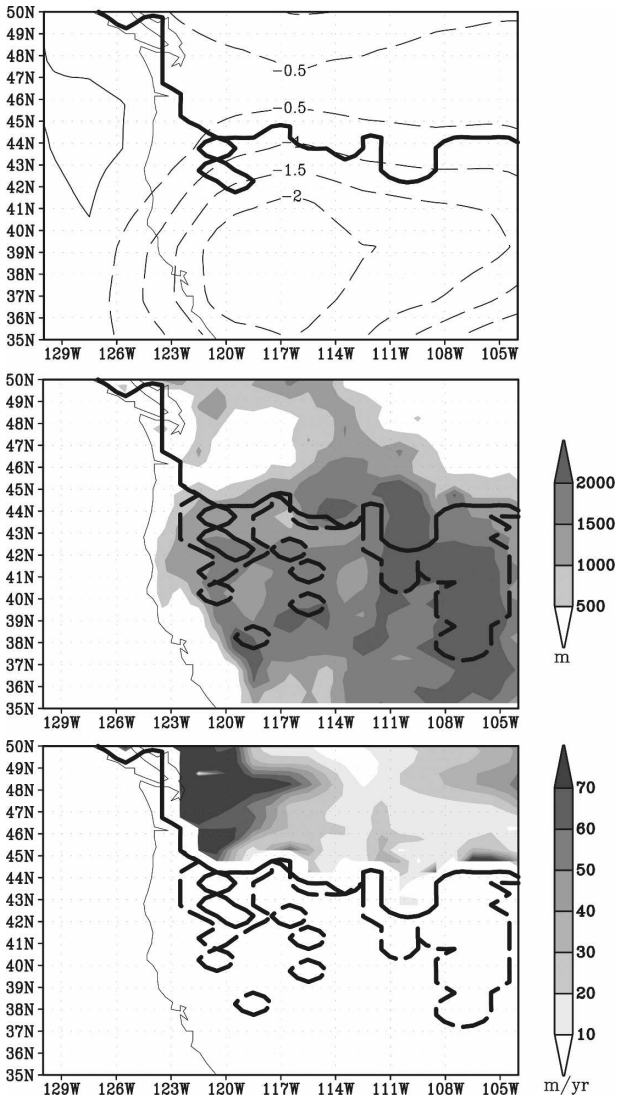

FIG. 14. Illustration of the dynamic feedback leading to ice growth along the cordillera in the INTERANN simulation. (top) Climatological sea level equivalent temperature anomaly for the first year in the interannual climate forcing record, showing a significant summertime cold anomaly during this year, south of the initial cordilleran ice margin (solid contour). Contour interval is 0.5 K. (middle) Bed topography in the same region, showing the southward extension of the ice sheet margin (dashed contour) collocated with high topography features during the first year of INTERANN. (bottom) Basal ice flow speeds adjacent to this newly formed ice, illustrating the potential for dynamic mass influx to the region of new ice growth that was initiated by interannual variability.

mass balance is shifted to more positive values. Owing to the above dynamical instability, the sensitivity of the ice sheet model to fully interannual climate forcing was much higher than its sensitivity to persistent climatological anomalies associated with ENSO phase extrema in the ENLN simulation.

d. Random interannual forcing

A final sensitivity study (INTERAND) was conducted to clarify the role of cold anomalies in the interannual climate forcing in initiating dynamic instability at the ice sheet margins. In INTERAND, the interannual variability in the AOGCM record used to drive INTERANN was replaced with spatially uncorrelated random noise about the climatological mean. Results from this experiment (not shown) exhibited the same pattern and degree of ice sheet growth as in INTERANN, indicating that dynamic instability at sensitive, high-altitude ice sheet margin model cells is triggered by interannual variability locally and is independent of the spatial extent of yearly cold anomalies in the interannual climate forcing.

5. Conclusions

We explored the sensitivity of an ice sheet model to interannual atmospheric variability through a series of targeted numerical ice sheet modeling experiments that incorporated increasingly complete subsets of interannual climate forcing from a 60-yr climate AOGCM LGM simulation. Results shed light on the relative sensitivity of a thermomechanic model of the Laurentide ice sheet to 1) the persistent (phase and annually averaged) component of ENSO, 2) seasonally modulated phase-averaged ENSO forcing, and 3) full interannual forcing that includes transient synoptic variability and transitions between ENSO phase extrema.

The GFDL AOGCM simulation of ENSO at the LGM is characterized by seasonal and interannual modulations of the midlatitude split jet stream that cause strong extratropical teleconnections over North America relative to present-day conditions, particularly during the winter season. Variations in the annual mean intensity of the split midlatitude jet stream during El Niño and La Niña dominate the annual-mean anomaly, changing the regional temperature and precipitation over North America and altering the local mass balance of the Laurentide ice sheet primarily at its northwestern and southeastern margins. Although qualitatively opposite in structure, the composite anomalies associated with ENSO extrema in the extratropics do not cancel out in the ENSO phase average owing to the nonlinearity of the ENSO cycle.

Idealized ice sheet simulations forced by a climatological LGM annual cycle perturbed uniformly throughout the year by annually averaged composites of phase-averaged ENSO exhibit weak sensitivity. When forced by the mean of ENSO phase extrema, the residual stationary influence in the average of El Niño

and La Niña teleconnections over North America drives small changes in ice thickness over 5 kyr. The simulated response of the Laurentide ice sheet to this climate forcing is a new equilibrium topographic state characterized by modest thinning at the northwest margin and thickening at the southeast margin, of approximately 5% compared to a control simulation.

The sensitivity of the ice sheet to phase-averaged ENSO climate forcing is reduced further when the seasonality of North American ENSO teleconnections is incorporated into the climate forcing. Since the dominant mass balance response of the ice sheet is ablative, weaker summertime ENSO composites (which are masked by stronger winter signals in the annual mean) exert a disproportionate control on the ice sheet response. Accordingly, a decreased sensitivity to phase-averaged ENSO perturbations was observed when the ice sheet model was forced by annual cycle climatology perturbed by monthly varying phase-averaged ENSO teleconnections. Idealized simulations forced in this fashion produced modest adjustments along the ice sheet margins less than 5% of the normal changes induced by the annual cycle over the course of 5 kyr.

In contrast to the simulations forced by interannually invariant phase-averaged ENSO climate perturbations, we find the ice sheet model to exhibit a much greater mass balance sensitivity when forced by an interannually varying climate record from the AOGCM. In this case, a new equilibrium state is attained over 5 kyr, entailing significant topographic readjustment along the western margins. We attribute the sensitive ice sheet response under fully interannual forcing to a dynamical mechanism at high-altitude ice sheet margins, which enables a net growth of the ice sheet volume by 33 M km^3 (an 11% increase) and area by 0.9 M km^2 (6% growth) solely due to transient interannual thermal anomalies in the climate forcing record. This internal dynamical response dominates any persistent impact of phase-averaged ENSO in the fully interannual simulation. Sensitivity studies using spatially uncorrelated random interannual variability produced similar results, indicating that this marginal ice sheet instability to interannual forcing can occur locally at susceptible ice sheet model cells, even in the absence of spatially coherent interannual thermal anomalies.

Several sources of uncertainty associated with the simplified climate parameterization for the ice sheet mass balance in this study warrant discussion. Degree-day melt factors are adopted from field and modeling studies in Greenland (Braithwaite 1995; Huybrechts and de Wolde 1999) and are not specifically tuned to the Laurentide ice sheet. However, studies on midlatitude alpine glaciers find similar degree-day melt factors (Jóhannesson et al. 1995; Braithwaite and Zhang 2000), suggesting that the energy balance conditions governing melt in Greenland are similar to those at midlatitudes. There is more uncertainty associated with the inherent limitations of degree-day melt modeling, which is unable to account for energy balance processes such as variations in shortwave and longwave radiation that accompany differences in cloud cover. Coupled ice sheet and climate models need to move to a fully coupled energy balance rather than parameterized temperature index models for snow and ice melt. This will also help to reduce uncertainties associated with the choice of temperature lapse rate; degree-day melt models are very sensitive to this choice when downscaling GCM temperatures in the ice sheet ablation area.

Additional uncertainty is inherent in the AOGCM interannual climate forcing record employed. Owing to computational constraints, there was a disparity in time scale between the available AOGCM simulation length (60 yr) and the millennial-scale (5 kyr) ice sheet integrations. Looping the 60-yr record necessarily introduces some uncertainty. For instance, a trend in the Niño-3.4 index in the AOGCM record may have been part of a centennial-scale variation that could have consequences for ice sheet mass balance, had a centennial scale AOGCM simulation been realizable. Furthermore, the coupling between the atmosphere and ice sheet in this study was one way; the response of an ice sheet to interannual atmospheric variability under two-way, interactive coupling remains an important open question.

In all, our simulations demonstrate that ice sheet models are, indeed, sensitive to interannual variations in climate forcing fields. Although this sensitivity is small for the persistent and seasonally modulated phase-averaged ENSO component of interannual variability, ISM sensitivity to fully interannual climate forcing is very significant due to a dynamical effect that triggers ice sheet advance during transient cool events adjacent to ice sheet margins over regions of high topography. Atmospheric thermal anomalies associated with interannual variability constitute a nonnegligible climate forcing on ice sheet models on millennial time scales and may play a nontrivial role during simulations of both glacial inception and glacial demise.

These findings are particularly relevant to the recent emergence and future development of the earth system modeling community's first interactively coupled ISM–GCMs (e.g., Ridley et al. 2005; Pritchard et al. 2008). The documented high ISM sensitivity to transient temperature anomalies in response to interannually varying climate forcing clearly merits further investigation. Since activating interannual variability in the climate

forcing fields caused the ISM to deviate significantly from its initial equilibrium topography (which was in line with geologic reconstructions for the LGM), a re-exploration of the optimal ISM parameter suite under interannual forcing is required. Such sensitivity studies will be an important precursor to future modeling explorations of the potential feedbacks between dynamic ice and year-to-year atmospheric variability.

Acknowledgments. This study was jointly funded by the Canadian Foundation for Climate and Atmospheric Sciences (Polar Climate Stability Project), the Canadian Institute for Advanced Studies (Earth System Evolution Program), and the National Sciences and Engineering Research Council of Canada. The authors made use of WestGrid computing resources, which are funded in part by the Canada Foundation for Innovation, Alberta Innovation and Science, BC Advanced Education, and the participating research institutions.

REFERENCES

AchutaRao, K., and K. R. Sperber, 2002: Simulation of the El Niño Southern Oscillation: Results from the Coupled Model Intercomparison Project. *Climate Dyn.,* **19,** 191–209.

An, S. I., and B. Wang, 2005: The forced and intrinsic low-frequency modes in the North Pacific. *J. Climate,* **18,** 876–885.

Berger, A., and M. F. Loutre, 1991: Insolation values for the climate of the last 10 million years. *Quat. Sci. Rev.,* **10,** 297–317.

Berger, W. H., and U. von Rad, 2005: Decadal to millennial cyclicity in varves and turbidites from the Arabian Sea: Hypothesis of tidal origin. *Global Planet. Change,* **34** (3–4), 313–325.

Braithwaite, R. J., 1995: Positive degree-day factors for ablation on the Greenland ice sheet studied by energy-balance modelling. *J. Glaciol.,* **41,** 153–160.

—— and Y. Zhang, 2000: Sensitivity of mass balance of five Swiss glaciers to temperature changes assessed by tuning a degree-day model. *J. Glaciol.,* **46,** 7–14.

Bromwich, D. H., E. R. Toracinta, H. Wei, R. J. Oglesby, J. L. Fastook, and T. J. Hughes, 2004: Polar MM5 simulation of the winter climate of the Laurentide ice sheet at the LGM. *J. Climate,* **17,** 3415–3433.

Bryan, K., 1969: A numerical method for the study of the circulation of the world ocean. *J. Comput. Phys.,* **3,** 347–376.

Bush, A. B. G., 2002: A comparison of simulated monsoon circulations and snow accumulation in Asia during the mid-Holocene and at the Last Glacial Maximum. *Global Planet. Change,* **32,** 331–347.

——, 2007: Extratropical influence of the El Niño–Southern Oscillation through the late Quaternary. *J. Climate,* **20,** 788–800.

——, and S. G. H. Philander, 1998: The role of ocean-atmosphere interactions in tropical cooling during the last glacial maximum. *Science,* **279,** 1341–1344.

——, and ——, 1999: The climate of the Last Glacial Maximum: Results from a coupled atmosphere-ocean general circulation model. *J. Geophys. Res.,* **104** (D29), 24 509–24 525.

CLIMAP, 1981: Seasonal reconstructions of the earth's surface at the last glacial maximum. Geological Society of America Map and Chart Series, Tech. Rep. MC-36, 17 pp.

DeWeaver, E., and S. Nigam, 2004: On the forcing of ENSO teleconnections by anomalous heating and cooling. *J. Climate,* **17,** 3225–3235.

Fairbanks, R. G., 1989: A 17,000-year glacio-eustatic sea level record: Influence of glacial melting rates on Younger Dryas event and deep-ocean circulation. *Nature,* **342,** 637–642.

Fanning, A. F., and A. J. Weaver, 1996: An atmospheric energy-moisture balance model: Climatology, interpentadal climate change, and coupling to an ocean general circulation model. *J. Geophys. Res.,* **101,** 15 111–15 128.

Goosse, H., and H. Renssen, 2004: Exciting natural modes of variability by solar and volcanic forcing: Idealized and realistic experiments. *Climate Dyn.,* **23,** 153–163.

Gordon, C. T., and W. Stern, 1982: A description of the GFDL global spectral model. *Mon. Wea. Rev.,* **110,** 625–644.

Hall, J. M., and L. H. Chan, 2004: Ba/Ca in benthic foraminifera: Thermocline and middepth circulation in the North Atlantic during the last deglaciation. *Paleoceanography,* **19,** PA4018, doi:10.1029/2004PA001028.

Hannachi, A., 2001: Toward a nonlinear identification of the atmospheric response to ENSO. *J. Climate,* **14,** 2138–2149.

Hostetler, S., N. Pisias, and A. Mix, 2006: Sensitivity of last glacial maximum climate to uncertainties in tropical and subtropical ocean temperatures. *Quat. Sci. Rev.,* **25** (11–12), 1168–1185.

Huybrechts, P., 1990: A 3-D model for the Antarctic ice sheet: A sensitivity study on the glacial-interglacial contrast. *Climate Dyn.,* **5,** 79–92.

——, and J. de Wolde, 1999: The dynamic response of the Greenland and Antarctic ice sheets to multiple-century climatic warming. *J. Climate,* **12,** 2169–2188.

——, J. Gregory, I. Janssens, and M. Wild, 2004: Modelling Antarctic and Greenland volume changes during the 20th and 21st centuries forced by GCM time slice integrations. *Global Planet. Change,* **42** (1–4), 83–105.

Jenssen, D., 1977: A three-dimensional polar ice sheet model. *J. Glaciol.,* **18,** 373–389.

Jòhannesson, T., O. Sigurdsson, T. Laumann, and M. Kennett, 1995: Degree-day glacier mass-balance modelling with application to glaciers in Iceland, Norway, and Greenland. *J. Glaciol.,* **41,** 345–358.

Kalnay, E., and Coauthors, 1996: The NCEP/NCAR 40-Year Reanalysis Project. *Bull. Amer. Meteor. Soc.,* **77,** 437–471.

Mahaffy, M. W., 1976: A three-dimensional numerical model of ice sheets: Tests on the Barnes Ice Cap, Northwest Territories. *J. Geophys. Res.,* **81** (B6), 1059–1066.

Marshall, S. J., and G. K. C. Clarke, 1997: A continuum mixture model of ice stream thermomechanics in the Laurentide ice sheet. 1. Theory. *J. Geophys. Res.,* **102** (B9), 20 599–20 613.

——, and P. U. Clark, 2002: Basal temperature evolution of North American ice sheets and implications for the 100-kyr cycle. *Geophys. Res. Lett.,* **29,** 2214, doi:10.1029/2002GL015192.

——, L. Tarasov, G. K. C. Clarke, and W. R. Peltier, 2000: Glaciological reconstruction of the Laurentide ice sheet: Physical processes and modelling challenges. *Can. J. Earth Sci.,* **37,** 769–793.

——, T. S. James, and G. K. C. Clarke, 2002: North American ice sheet reconstructions at the Last Glacial Maximum. *Quat. Sci. Rev.,* **21,** 175–192.

Mysak, L. A., R. G. Ingram, J. Wang, and A. van der Baaren, 1996: The anomalous sea-ice extent in Hudson Bay, Baffin

Bay and the Labrador Sea during three simultaneous NAO and ENSO episodes. *Atmos.–Ocean,* **34,** 313–343.

Newman, M., G. P. Compo, and M. A. Alexander, 2003: ENSO-forced variability of the Pacific decadal oscillation. *J. Climate,* **16,** 3853–3857.

Otto-Bliesner, B. L., S. J. Marshall, J. T. Overpeck, G. H. Miller, and A. Hu, 2006: Simulating Arctic climate warmth and ice field retreat in the last interglaciation. *Science,* **311,** 1751–1753.

Pacanowski, R. C., and S. G. H. Philander, 1981: Parameterization of vertical mixing in numerical models of tropical oceans. *J. Phys. Oceanogr.,* **11,** 1443–1451.

——, K. Dixon, and A. Rosati, 1991: The GFDL modular ocean model user guide. Geophysical Fluid Dynamics Laboratory Tech. Rep. 2, 17 pp.

Peltier, W. R., 1985: The LAGEOS constraint on deep mantle viscosity: Results from a new normal mode method for the inversion of viscoelastic relaxation spectra. *J. Geophys. Res.,* **90,** 9411–9421.

——, 1994: Ice-age paleotopography. *Science,* **265,** 195–201.

——, and L. P. Solheim, 2004: The climate of the earth at Last Glacial Maximum: Statistical equilibrium state and a mode of internal variability. *Quat. Sci. Rev.,* **23** (3–4), 335–357.

Pritchard, M. S., A. B. G. Bush, and S. J. Marshall, 2008: Neglecting ice-atmosphere interactions underestimates ice sheet melt in millennial-scale deglaciation simulations. *Geophys. Res. Lett.,* **35,** L01503, doi:10.1029/2007GL031738.

Rasmusson, E. M., and T. H. Carpenter, 1982: Variations in tropical sea surface temperature and surface wind fields associated with the Southern Oscillation/El Niño. *Mon. Wea. Rev.,* **110** (5), 354–384.

Ridley, J. K., P. Huybrechts, J. M. Gregory, and J. A. Lowe, 2005: Elimination of the Greenland ice sheet in a high CO_2 climate. *J. Climate,* **18,** 3409–3427.

Rodgers, K. B., G. Lohmann, S. Lorenz, R. Schneider, and G. M. Henderson, 2003: A tropical mechanism for Northern Hemisphere deglaciation. *Geochem. Geophys. Geosyst.,* **4,** 1046, doi:10.1029/2003GC000508.

——, and Coauthors, 2004: Sensitivity of Northern Hemispheric continental ice sheets to tropical SST during deglaciation. *Geophys. Res. Lett.,* **31,** L02206, doi:10.1029/2003GL018375.

Rosenthal, Y., and A. J. Broccoli, 2004: In search of paleo-ENSO. *Science,* **304,** 219–221.

Schneider, N., and B. D. Comuelle, 2005: The forcing of the Pacific decadal oscillation. *J. Climate,* **18,** 4355–4373.

Shin, S. I., Z. Liu, B. Otto-Bliesner, E. C. Brady, J. E. Kutzbach, and S. P. Harrison, 2003: A simulation of the Last Glacial Maximum climate using the NCAR-CCSM. *Climate Dyn.,* **20** (2–3), 127–151.

Slonosky, V. C., L. A. Mysak, and J. Derome, 1997: Linking Arctic sea-ice and atmospheric circulation anomalies on interannual and decadal timescales. *Atmos.–Ocean,* **35,** 333–366.

Stott, L., C. Poulsen, S. Lund, and R. Thunell, 2002: Super ENSO and global climate oscillations at millennial time scales. *Science,* **297,** 222–226.

Straus, D. M., and J. Shukla, 2002: Does ENSO force the PNA? *J. Climate,* **15,** 2340–2358.

Trenberth, K. E., 1997: The definition of El Niño. *Bull. Amer. Meteor. Soc.,* **78,** 2771–2777.

——, J. M. Caron, D. P. Stepaniak, and S. Worley, 2002: Evolution of El Niño–Southern Oscillation and global atmospheric surface temperatures. *J. Geophys. Res.,* **107,** 4065, doi:10.1029/2000JD000298.

Tudhope, A. W., and Coauthors, 2001: Variability in the El Niño Southern Oscillation through a glacial-interglacial cycle. *Science,* **291,** 1511–1517.

Van der Avoird, E., H. A. Djikstra, J. J. Nauw, and C. J. E. Schuurmans, 2002: Nonlinearly induced low-frequency variability in a midlatitude coupled ocean-atmosphere model of intermediate complexity. *Climate Dyn.,* **19** (3–4), 303–320.

Wang, X., A. S. Auler, R. L. Edwards, H. Cheng, P. S. Cristaili, P. L. Smart, D. A. Richards, and C.-C. Shen, 2004: Wet periods in northeastern Brazil over the past 210 kyr linked to distant climate anomalies. *Nature,* **432,** 740–743.

Wu, A., and W. W. Hsieh, 2004: The nonlinear patterns of North American winter temperature and precipitation associated with ENSO. *J. Climate,* **18,** 1736–1752.

Wu, P., and W. R. Peltier, 1982: Viscous gravitational relaxation. *Geophys. J. Roy. Astron. Soc.,* **70,** 435–485.

Yin, J. H., and D. S. Battisti, 2001: The importance of tropical sea surface temperature patterns in simulations of Last Glacial Maximum climate. *J. Climate,* **14,** 565–581.